Supplemental Information for:

Asymmetric Distribution of Lunar Impact Basins Caused by Variations in Target Properties

Katarina Miljković*, Mark A. Wieczorek, Gareth S. Collins, Matthieu Laneuville, Gregory A. Neumann, H. Jay Melosh, Sean C. Solomon, Roger J. Phillips, David E. Smith and Maria T. Zuber

*correspondence to: miljkovic@ipgp.fr

This PDF includes:

1. Supplementary Text
2. References (33-54)
3. Figs. S1 to S4
4. Tables S1 to S5

1 Evidence for a hemispheric asymmetry in basin sizes

In our analysis we considered large impact basins that possess unambiguous signatures of crustal thinning in the GRAIL-derived crustal thickness model (*9*). Basins with crustal thinning diameters, D, less than 200 km were not analyzed in order to minimize preservation biases that might result from burial by mare basalts or ejecta from adjacent basins, or from deficiencies in the crustal thickness model. Azimuthally averaged crustal thickness profiles were generated, and the diameters of crustal thinning determined from the radial distance from basin center at which the crustal thickness first reaches its pre-impact value (*1, 2*) (Table S1). The pre-impact crustal thickness, H, was taken as the average value at a distance of three basin radii from the basin center.

Table S1. Location, diameter of crustal thinning D, and pre-impact crustal thickness H, for basins with diameter greater than 200 km. Stratigraphic ages correspond to the Imbrian (I), Nectarian (N), and pre-Nectarian (PN).

Basin name	(°E, °N)	D, km	H, km	Age (*3*)	Relative age (*35, 36*)
Nearside					
Imbrium	$(341, 37)$	680	28	I	3
Serenitiatis	$(19, 25)$	607	28	PN	4 (uncertain)
Crisium	$(59, 17)$	476	31	N	4
Smythii	$(87, -1)$	465	35	PN	11
Nectaris	$(34, -16)$	434	34	N	6
Humorum	$(321, -24)$	380	31	N	4
Asperitatis	$(27, -8)$	370	34	-	-
Humboldtianum	$(83, 58)$	325	31	N	4
Cruger-Sirsalis	$(293, -16)$	270	35	PN	1-7 (uncertain)
Humboldt	$(82, -27)$	235	31	-	-
C25 (*37*)	$(351, 11)$	235	34	-	-
Schiller-Zucchius	$(315, -56)$	209	35	PN	9
Farside					
Orientale	$(266, -19)$	418	43	I	1
Moscoviense	$(148, 26)$	319	42	N	6
Freundlich-Sharanov	$(175, 19)$	308	44	PN/N	8
Coulomb-Sarton	$(237, 54)$	305	42	PN	11
Fitzgerald-Jackson	$(192, 25)$	303	49	PN	-
Mendel-Rydberg	$(265, -50)$	286	41	N/PN	6
T22 (*37*)	$(179, 49)$	281	45	-	-
Apollo	$(209, -36)$	276	24	PN/N	7
Hertzsprung	$(231, 2)$	252	54	N/PN	4
Compton-Belkovitch	$(105, 61)$	230	29	-	-
Korolev	$(202, -5)$	223	57	N/PN	6
Dirichlet-Jackson	$(201, 13)$	214	56	PN	-

The cumulative number of basins with diameters greater than D is plotted in Fig. 2 for both the nearside and farside hemispheres. We note that there are 12 basins with diameters greater than 200 km on each hemisphere, and nine basins with diameters greater than 250 km on each hemisphere, consistent with the hypothesis of a globally uniform impact flux. Nevertheless, Fig. 2 shows that the size distributions for the two hemispheres differ significantly. With increasing diameter, the number of basins on the farside drops considerably faster than that for the nearside. For $D > 320$ km there are eight basins on the nearside and only one on the farside. The probability that such a distribution of basins would occur by chance under the assumption of a uniform impact flux is quantified in Fig. S1. The total number of basins with diameters greater than a specific value was first determined, and the probability that the number of basins on the nearside would be greater than or equal to the observed value was calculated from the binomial distribution. For diameters greater than or equal to 320 km, there is less than a 2% probability that such a distribution could have occurred by chance. Though the probability increases at large D, this result is simply a reflection of the fact that the total number of basins decreases with increasing diameter. Previous studies of the Moon's impact bombardment by near-Earth asteroids show that the cratering rate between the nearside and farside hemispheres should be similar (*12, 33, 34*) for a large range of impact conditions.

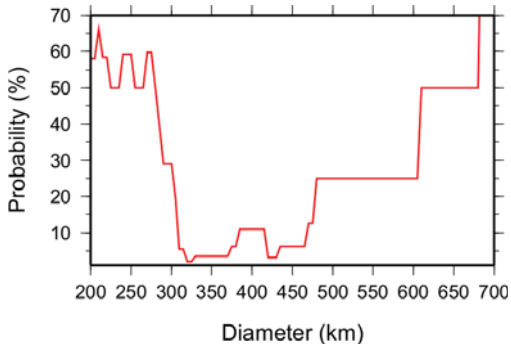

Fig. S1. Probability that the number of basins on the nearside hemisphere of the Moon with diameter greater than D would be as great or greater than the observed value.

The impact basins with crustal thickness signatures in this study correspond to approximately the youngest half of the entire inventory of lunar basins. Among the 15 relative age groups of Wilhelms (*35*) these basins are all younger than or contemporaneous with group 11. Globally, there is a total of about 27 basins that formed with ages less than or equal to group 11, and about 19 that are older (*36*). Stratigraphically, seven of the basins with crustal thickness signatures formed in the Imbrian and Nectarian periods, five during the Nectarian or pre-Nectarian, and seven during the pre-Nectarian (*3*). The youngest basin in our study, Orientale, is estimated to have formed 3.73 Ga (billion years ago) (*12*) and an upper limit on the beginning of the Nectarian period is about 4.2 Ga (*11*). The South Pole-Aitken basin was excluded from consideration in our study given that it is the oldest impact structure on the Moon (it is the sole

member of group 15 of Wilhelms), and because the thermal regime of the crust and underlying mantle at the time it formed is highly uncertain.

In addition to the impact basins utilized in this study, we note that there are three large basins with ambiguous crustal thickness signatures: Australe (94° E, 34° S, D=600±300 km), Nubium (343° E, 21° S, D=700±200 km), and Fecunditatis (52° E, 5° S, D=450±250 km). These three basins are all located on the nearside hemisphere and are older than those basins with known relative ages in Table S1. Inclusion of these basins in our study would have made the asymmetry in impact basin sizes even more pronounced.

2 Impact modelling setup

iSALE-2D (*21–23*) is a multi-material and multi-rheology finite difference shock physics code used for simulating impact processes. The code has been benchmarked against other hydrocodes (*38*). A half-space target mesh was divided into two horizontal layers, the crust and the mantle, and cylindrical symmetry is assumed. The horizontal and vertical cell size was varied between 0.5×0.5 and 1.5×1.5 km, depending on the impactor size. The choice of the cell size did not affect the results, as (a factor of 3) lower-resolution simulations (used for testing and not included here) also gave similar crust-mantle profiles and, most importantly, the same crustal thinning diameters.

The pre-impact thickness of crustal materials was fixed at either 30 km (corresponding to the nearside) or 60 km (corresponding to the maximum thickness of the farside highlands). The impact speed was taken to be 10 or 17 km s^{-1} to accommodate a wide distribution of expected impact speeds during the epoch of basin formation (*40*), and the impactors (assumed to be made of dunite) ranged from 15 to 90 km in diameter in order to generate basins comparable in size to the observed lunar basins. These impact speeds could also represent moderately oblique incidence angles, because the vertical component of velocity vector mainly controls the final basin diameter (*41*). A lunar surface gravitational acceleration of 1.62 m s^{-2} was used. To allow faster computation, low-density material (<50–300 kg m^{-3}) that largely represents vaporized material was removed from simulations, as it does not contribute to the basin formation process (*7*). The simulations were stopped 2 hours after impact. Temperatures beneath the basin were still elevated at that time, but the depth to the crust-mantle interface and the total crustal thickness are not expected to change markedly during further cooling (*42*).

The material models for the crust, mantle, and impactor use the ANEOS-derived equation of state (EOS) tables, as well as strength (*22*), failure, and thermal softening models for basalt and dunite that were used in previous studies (*24, 25*) for modelling basin formation on the Moon and Mars (Table S2). These material parameters are similar to the ones used in other previous impact modelling studies that involved lunar mantle (*42, 43*). It was found in this study (by replacing basalt with granite) and other studies (*42*) that the choice of EOS for the crustal material does not make a substantial difference in the outcome of a basin-forming event.

In this study, the role of temperature is restricted to its effect on the shear strength. The

material shear strength model in iSALE includes a description of thermal softening (*22, 44*):

$$Y = Y_c \tanh\left[\epsilon(T_m/T - 1)\right], \tag{1}$$

where Y_c is is the cold shear strength, ϵ is a material constant, T is temperature, and T_m is the melting temperature. In this model, the strength decreases with temperature and is zero at, and above, the solidus. Because the solidus is not defined by the equation of state tables, we use the Simon approximation to fit the pressure dependence for the melting temperature of anhydrus basalt and KTB peridotite (*45, 46*) for the crust and mantle, respectively:

$$T_m = T_{m,0}\ (p/a + 1)^{1/c}\,, \tag{2}$$

where $T_{m,0}$ is the melt temperature at zero pressure, p is pressure, and a and c are material constants.

Even though ANEOS is the best available representation of a multi-phase geological material, one limitation of the current ANEOS code for both materials is that it does not include the latent heat of melting at the transition between solid and liquid. For this reason, the temperatures in the table above the solidus are overestimated when the rock is molten. However, as accurate melt volume calculations are not the focus of this study, this limitation is not important.

Simulations employ the block-oscillation model of acoustic fluidization (*46–48*) to facilitate crater collapse, which is important for cooler targets. A range of acoustic fluidization parameters were tested and varied until a basin forming in a cooler target collapsed into a final basin morphology with an acceptable basin depth (5-10 km) after the simulation ended. These parameters are also similar to the ACFL parameters employed in the simulations of Chicxulub crater collapse (*49*). Subsequent long-term cooling and relaxation of a basin over millions of years could cause the uplift of the complete basin for another few kilometers, essentially compensating for this depth (*42*).

Although GRAIL has revealed that the lunar crust has an average porosity of 7-12%, for simplicity we did not employ iSALE's porosity compaction model (*23*) in our simulations because we do not expect porosity compaction to play an important role in large basin formation (as this is driven by uplift of deep mantle rocks with little porosity) and, as far as the data show, no major nearside-farside difference in porosity is observed. Including crustal pore-space compaction would enhance shock heating of the crustal rocks in the basin center and dissipate the shock wave in the crust, possibly resulting in a slightly smaller crater.

The input parameters to our simulations are provided in Table S2. The material model uses customized vertical thermal profiles of crust and upper mantle, as described in the following section.

Table S2. Target material parameters for iSALE-2D numerical models of impact basin formation.

Description	Crust	Mantle and Impactor
Equation of state	Basalt ANEOS	Dunite ANEOS
Melt temperature at zero pressure (K), $T_{m,0}$	1360	1436
Constant in thermal softening law, ϵ	0.7	2.0
Constant in Simon approximation (GPa), a	4.5	1.4
Exponent in Simon approximation, c	3.0	5.0
Poisson's ratio	0.25	0.25
Cohesion (damaged) (MPa)	0.01	0.01
Coefficient of internal friction for material (damaged)	0.6	0.6
Limiting strength at high pressure (damaged) (GPa)	2.5	3.5
Cohesion (intact) (MPa)	20	50
Coefficient of internal friction for material (intact)	1.4	1.5
Limiting strength at high pressure (intact) (GPa)	2.5	3.5
Minimum failure strain for low pressure states	10^{-4}	10^{-4}
Increase in failure strain with pressure	10^{-11}	10^{-11}
Pressure above which failure is always compressional (MPa)	0.3	0.3
γ_η constant	0.004	0.004
γ_β constant	230	230
Peak vibrational velocity as a fraction of the peak particle velocity	0.1	0.1

3 Lunar thermal evolution modelling

The three-dimentional (3D) spherical, finite-volume thermo-chemical convection code GAIA (*26*) was used to simulate the thermal evolution of the Moon. Our simulations, described by (*20*), follow previous work (*15*) by including an asymmetric distribution of heat sources as implied by orbital gamma-ray remote sensing measurements (*50*). To simulate the effects of the enhanced heat production from the Procellarum KREEP Terrane (*13, 14*) on the nearside hemisphere of the Moon, the equivalent of a 10-km-thick layer of KREEP basalt was placed in a spherical cap with an angular radius of 40°. For one model, the 10-km layer of enhanced heat production was placed just beneath a 40-km-thick crust (model PKT1), whereas for the other model, the equivalent of 10 km of KREEP basalt was distributed over the entire 40 km of crust (model PKT2). Our model has a bulk silicate abundance of 25 ppb uranium, which is comparable to the bulk silicate value on Earth.

GAIA solves the standard hydrodynamics equations for an incompressible fluid, with an infinite Prandtl number under the Boussinesq approximation. Both core cooling and radioactive decay are included. The viscosity η is taken to be Newtonian. Mantle melting is considered through the consumption of latent heat in the energy equation, and melt is assumed to leave the system instantaneously so that no latent heat of crystallization is released later. The solidus, $T_{\rm sol}$, and liquidus, $T_{\rm liq}$, are taken to be those of KLB-1 peridotite (*51*), and the density and depletion of the mantle (cumulative melt fraction) is tracked using a composition field.

Two initial temperature profiles were considered for the lunar thermo-chemical evolution. For the first model, M1, the initial temperature follows the solidus in the uppermost 350 km

of the mantle and an adiabatic gradient below (*52*). Conceptually, the region at the solidus represents the upper portion of the solidified magma ocean that did not convectively readjust, whereas the lower portion of the mantle underwent rapid convection. The second model, M2, used an adiabatic profile for the entire mantle (*15*), which corresponds to a well-mixed, initially convecting interior. In contrast to spherically symmetric thermal evolution models, for which the global cooling rate dictates the mantle behavior, the high heat production associated with the PKT dominates the thermal models here. The PKT heats the underlying mantle and gives rise to a shallow temperature peak for the nearside temperature profiles (Fig. S2). The farside is nearly unaffected by the PKT region, and its thermal evolution follows approximately a conductive state. On the nearside, regardless of the initial mantle temperature profile employed, models with the heat production enhancement below the crust (PKT1) give rise to a strong peak in temperature in the upper mantle. The model with the enhanced heat production uniformly distributed within the crust (PKT2) does not have such a peak as a result of the higher rate of heat loss to space, but it is still considerably hotter than the farside hemisphere.

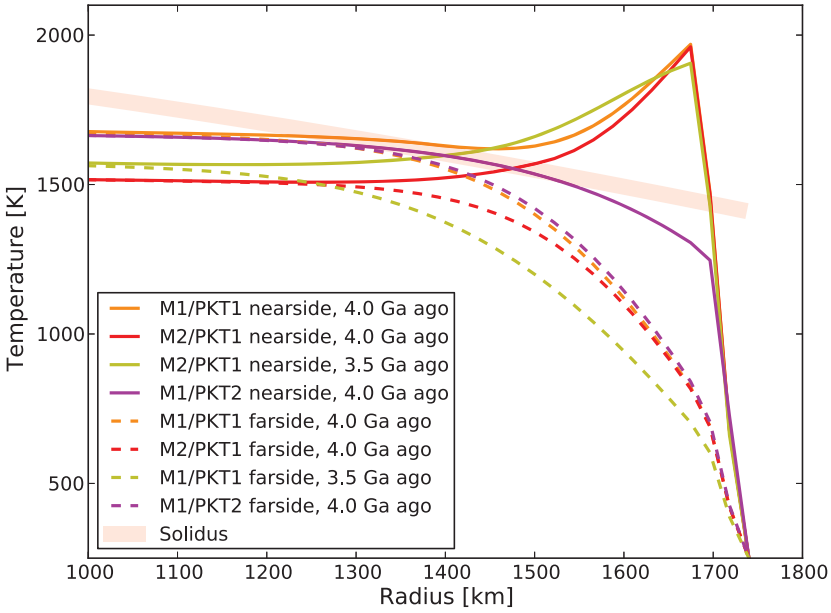

Fig. S2. Vertical temperature profiles used in the impact simulations. Nearside and farside temperature profiles are shown with solid and dotted curves, respectively. M1 and M2 correspond to two different initial mantle temperature profiles; PKT1 and PKT2 include the enhanced heat production at the base of the nearside crust or distributed uniformly within the nearside crust, respectively. The temperature profiles for the upper mantle and crust on the farside are not affected by the nearside Procellarum KREEP Terrane.

The different temperature profiles used in our impact simulations correspond to the modeled thermal state after 0.5 billion years of evolution (i.e., 4 Ga). We also investigated an additional temperature profile for M2/PKT1 corresponding to 3.5 Ga, which is about 200 million years younger than Orientale. This additional model was included to show that the temperature effects persisted over a long time period (comparable to the duration of the basin-formation epoch) and how small changes in temperature profiles over this time would affect basin formation.

4 Impact modelling results

The parameters used in the iSALE impact simulations presented in Fig. 4 are shown in Tables S3 and S4. The relation in Fig. 4 (reprinted with additional annotations and data in Fig. S3) between thin and thick crust for the same temperature profile is

$$D_{\mathrm{thin}} = 1.317\, D_{\mathrm{thick}}^{0.957}, \tag{3}$$

where D is in km. This relation demonstrates that crustal thickness has little effect on the size of the final region of crustal thinning, as this relationship is very close to $D_{thin}/D_{thick} \approx 1$. Nevertheless, the absolute thickness of crustal material in the basin center, as well as the amount of excavated mantle material, depends on the pre-impact crustal thickness.

The relations between crustal thinning on a hot nearside and that on the cool farside for different temperature profiles are:

$$D_{\mathrm{farside}} = 4.527\, D_{\mathrm{nearside}}^{0.836}, \quad \text{M1/PKT1 (4.0 Ga)} \tag{4}$$

$$D_{\mathrm{farside}} = 1.247\, D_{\mathrm{nearside}}^{1.015}, \quad \text{M2/PKT1 (4.0 Ga)} \tag{5}$$

$$D_{\mathrm{farside}} = 4.630\, D_{\mathrm{nearside}}^{0.829}, \quad \text{M2/PKT1 (3.5 Ga)} \tag{6}$$

$$D_{\mathrm{farside}} = 0.796\, D_{\mathrm{nearside}}^{1.081}, \quad \text{M1/PKT2 (4.0 Ga).} \tag{7}$$

The differences in crustal thinning between the nearside and farside are greatest for the hottest nearside temperature profile at 4 Ga (M1/PKT1, shown in orange in Fig. S3). This relation is very similar to that for the temperature profiles M2/PKT1 at 3.5 Ga (yellow in Fig. S3). This similarity demonstrates that our results are not critically dependent on the assumed time of basin formation, because even for a step as big as 0.5 Gyr the temperature effects persisted. In addition, Table S4 and Fig. S3 include impact modelling results for two different impact speeds, 10 and 17 km s^{-1}. Under such a change in impact speeds, the relation between nearside and farside thinning diameters does not change, indicating that Eqs. (4)-(7) are largely independent of impact conditions.

Table S3. Impact simulation parameters used in Figs. 4 and S3 for the dependence on crustal thickness. L is the projectile size, v is the impact velocity, and D is the diameter of crustal thinning for a thick (60 km) or thin (30 km) crust. All thermal profiles correspond to the farside at 4 Ga. On the farside, M1/PKT1 is equal to M1/PKT2 and M2/PKT1 is equal to M2/PKT2, which means that the temperature increase characteristic for the nearside has no influence on the farside.

L (km)	v (km s^{-1})	Temperature profile	D_{thick} (km)	D_{thin} (km)
30	17	M1/PKT1	155	166
30	17	M2/PKT1	159	167
45	17	M1/PKT1	244	256
45	17	M2/PKT1	262	265
60	17	M1/PKT1	334	346

Table S4. Impact simulation parameters used in Figs. 4 and S3 for the dependence on temperature. L is the projectile size, v is the impact velocity, and D is the diameter of crustal thinning on a thin nearside and thick farside crust. Temperature profiles are noted in time before present.

L, km	v, km s^{-1}	Temperature profile	D_{farside}, km	D_{nearside}, km
30	17	M1/PKT1 (4.0 Ga)	155	315
45	17		244	433
60	17		334	572
90	17		470	797
45	17	M2/PKT1 (4.0 Ga)	262	359
60	17		334	450
90	17		442	610
15	17	M2/PKT1 (3.5 Ga)	77	154
60	17		307	538
90	17		421	684
15	10		43	110
45	10		160	328
60	10		226	420
30	17	M1/PKT2, (4.0 Ga)	155	184
45	17		244	312
60	17		334	420

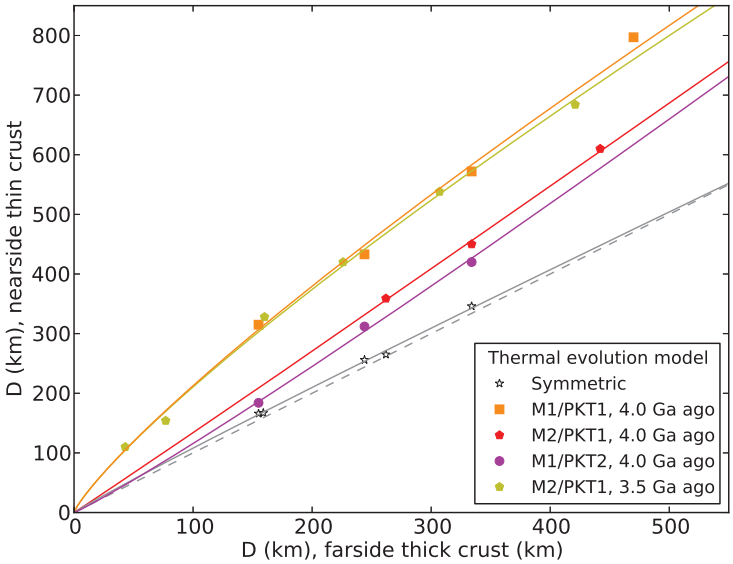

Fig. S3. Dependence of impact basin size on target properties (from Fig. 4 with additional annotations and data). The diameter of crustal thinning for impact on a thin and hot nearside crust is plotted as a function of the corresponding diameter on a thick and cool far side crust. Simulations using the same temperature profile for the two hemispheres are shown in grey, whereas simulations with a hot nearside temperature profile resulting from the Procellarum KREEP Terrane are shown in other colors. Points of the same color correspond to simulations with different projectile diameters. The employed temperature profiles are given in Fig. S2. The dashed gray line marks a ratio of 1:1.

The three vertical columns A, B, and C in Fig. S4 show series of snapshots from iSALE-2D impact simulations for the first 2 h after impact. All impacts were modelled with a 45-km-impactor at 17 km s^{-1} vertical impact velocity into: (A) 60-km-thick and cold farside crust, (B) 30-km-thick and cold farside, and (C) 30-km-thick and hot nearside crust. The temperature profile for A and B was M1/PKT2 (which is the same as M1/PKT1, as the PKT anomaly does not affect the thermal state of the farside) and for C it was M1/PKT2 (Fig. S2). Crust and mantle are represented by material concentration within the numerical mesh, which remains the same after the basin has cooled. The abscissa shows basin radius, in km, and the ordinate shows basin depth, in km, starting at the pre-impact surface taken as the zero-level. The values for the diameters of crustal thinning, D, for cases A, B, and C are in Tables S3 and S4. The first row of snapshots shows cratering initiation, the second row shows opening of the transient cavity and the latter is followed by a rapid crater floor rebound (third row). The fourth row shows the approximate maximum crater floor rebound, which is followed by collapse into a basin inner ring, as shown in the subsequent rows. The diameter of crustal thinning is marginally affected by different crustal thicknesses, considering that the diameter is measured as the radial distance from basin center at which the crustal thickness is first equal to the pre-impact crustal thickness.

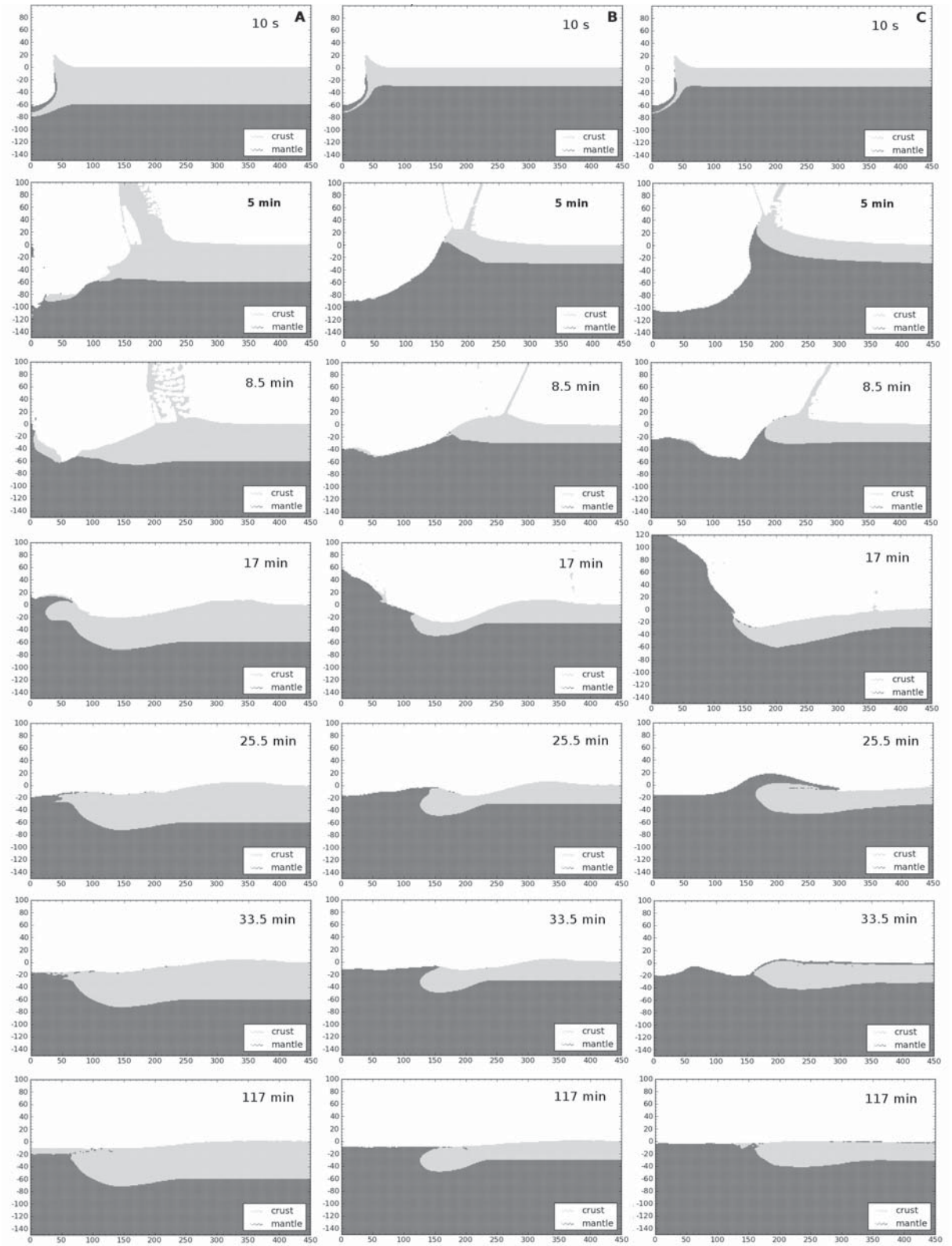

Fig. S4. Snapshots from three iSALE-2D impact simulations, for the same impact conditions and different target properties. (A) Impact into thick crust corresponding to the cold farside highlands; (B) Impact into thin crust corresponding to the cold farside (e.g. South Pole-Aitken basin floor); (C) Impact into thin crust corresponding to the hot nearside hemisphere (PKT and mare-affected regions).

This study was conducted only for a vertical impact scenario. Statistically more probable oblique impact scenarios would require 3D simulations that are computationally challenging. Because this work is a comparative study of basin formation on the nearside and farside hemispheres, and no variation of impact angle is expected between the hemispheres, we did not consider impact angle as an important parameter. However, we have performed a few oblique impact simulations in iSALE-3D (*53–55*) for both nearside and farside targets at 30^o and 45^o impact angles (measured from the horizontal). Although lowering the impact angle does systematically reduce the size of the transient crater (as expected from crater scaling presented in (*54*)), and hence the amount of uplift and the diameter of the region of crustal thinning, this trend was observed for basins on both hemispheres and so does not affect our conclusions.

5 Rescaling of the largest lunar impact basins

With the relations in Eqs. (4)-(7), we determined the size that the nearside basins would have if they had formed on a cold farside crust (Table S5). This procedure is necessarily approximate as the subsurface temperature distribution is uncertain, because it depends on time, distance from the Procellarum KREEP Terrane, and the conditions that followed magma ocean crystallization. Regardless, we expect that our temperature profiles should compensate for the first-order differences between the nearside and farside hemispheres. Considering that the Imbrium (341° E, 37° N), Serenitatis (19° E, 26° N), and C25 (351° E, 11° N) basins lie largely within the PKT, those basins were corrected using the hottest considered nearside temperature profile (M1/PKT1). The remainder of the nearside basins, which are all adjacent to mare deposits, were corrected using the coolest of the three considered nearside temperature profiles (M1/PKT2).

Table S5. Diameter of crustal thinning $D_{obs.}$ for the nearside and farside basins. Also listed for the nearside basins is the corresponding diameter $D^\star$ if the basin had formed in crust with the same temperature profile as the farside. Entries in bold correspond to those shown in Fig. 2.

Nearside basin	$D_{\rm obs}$	$D^\star$			Farside basin	$D_{\rm obs}$
		M1/PKT1	M2/PKT1	M1/PKT2		
Imbrium	680	**402**	497	514	Orientale	418
Serenitiatis	607	**350**	444	463	Moscoviense	319
Crisium	476	262	350	**370**	Freundlich-Sharanov	308
Smythii	465	255	342	**362**	Coulomb-Sarton	305
Nectaris	434	235	319	**339**	Fitzgerald-Jackson	303
Humorum	380	200	280	**300**	Mendel-Rydberg	286
Asperitatis	370	194	273	**293**	T22	281
Humboldtianum	325	166	240	**260**	Apollo	276
Cruger-Sirsalis	270	133	200	**219**	Hertzsprung	252
Humboldt	235	113	174	**192**	Compton-Belkovitch	230
Schiller-Zucchius	209	98	155	**173**	Korolev	223
C25	235	**113**	174	192	Dirichlet-Jackson	214

References

1. Wieczorek, M. A., Phillips, R. J. Lunar multiring basins and the cratering process. *Icarus* **139**, 246–259 (1999).

2. Hikida, H., Wieczorek, M. A. Crustal thickness of the Moon: New constraints from gravity inversions using polyhedral shape models. *Icarus* **192**, 150–166 (2007).

3. Fassett, C. I. *et al.* Lunar impact basins: Stratigraphy, sequence and ages from superposed impact crater populations measured from Lunar Orbiter Laser Altimeter (LOLA) data. *J. Geophys. Res.* **117**, E00H06 (2012).

4. Turtle, E. P. *et al.* Impact structures: What does crater diameter mean? In *Large Meteorite Impacts III* (eds. Kenkmann, T., Hörz, F., Deutsch, A.), pp. 1–24, Spec. Paper 384 (Geological Society of America, Boulder, Colo., 2005).

5. Neumann, G. A., Zuber, M. T., Smith, D. E., Lemoine, F. G. The lunar crust: Global structure and signature of major basins. *J. Geophys. Res.* **101**, 16,841–16,863 (1996).

6. Bratt, S. R., Solomon, S. C., Head, J. W., Thurber, C. H. The deep structure of lunar basins: Implications for basin formation and modification. *J. Geophys. Res.* **90**, 3049–3064 (1985).

7. Potter, R., Kring, D. A., Collins, G. S., Kiefer, W., McGovern, P. Estimating transient crater size using the crustal annular bulge: Insights from numerical modeling of lunar basin-scale impacts. *Geophys. Res. Lett.* **39**, L18203 (2012).

8. Zuber, M. T. *et al.* Gravity field of the Moon from the Gravity Recovery and Interior Laboratory (GRAIL) mission. *Science* **339**, 668–671 (2013).

9. Wieczorek, M. A. *et al.* The crust of the Moon as seen by GRAIL. *Science* **339**, 671–675 (2013).

10. Norman, M. D., Duncan, R. A., Huard, J. J. Imbrium provenance for the Apollo 16 Descartes terrain: Argon ages and geochemistry of lunar breccias 67016 and 67455. *Geochim. Cosmochim. Acta* **74**, 763–783 (2010).

11. Fernandes, V. A., Fritz, J., Weiss, B. P., Garrick-Bethell, I., Shuster, D. L. The bombardment history of the Moon as recorded by ^{40}Ar–^{39}Ar chronology. *Meteorit. Planet. Sci.* **48**, 241–269 (2013).

12. Le Feuvre, M., Wieczorek, M. A. Nonuniform cratering of the Moon and a revised crater chronology of the inner Solar System. *Icarus* **214**, 1–20 (2011).

13. Jolliff, B. L., Gillis, J. J., Haskin, L. A., Korotev, R. L., Wieczorek, M. A. Major lunar crustal terranes: Surface expressions and crust-mantle origins. *J. Geophys. Res.* **105**, 4197–4216 (2000).

14. Korotev, R. L. The great lunar hot spot and the composition and origin of the Apollo mafic ("LKFM") impact-melt breccias. *J. Geophys. Res,* **105**, 4317–4346 (2000).

15. Wieczorek, M. A., Phillips, R. J. The "Procellarum KREEP Terrane": Implications for mare volcanism and lunar evolution. *J. Geophys. Res.* **105**, 20,417–20,430 (2000).

16. Solomon, S. C., Comer, R. P., Head, J. W. The evolution of impact basins: Viscous relaxation of topographic relief. *J. Geophys. Res.* **87**, 3975–3992 (1982).

17. Kamata, S. *et al.* Viscoelastic deformation of lunar impact basins: Implications for heterogeneity in the deep crustal paleo-thermal state and radioactive element concentration. *J. Geophys. Res.* **118**, 398–415 (2013).

18. Zhong, S., Parmentier, E. M., Zuber, M. T. A dynamic origin for the global asymmetry of lunar mare basalts. *Earth Planet. Sci. Lett.* **177**, 131–140 (2000).

19. Hess, P. C., Permentier, E. M. Thermal evolution of a thicker KREEP liquid layer. *J. Geophys. Res.* **106**, 28,023–28,032 (2001).

20. Laneuville, M., Wieczorek, M. A., Breuer, D., Tosi, N. Asymmetric thermal evolution of the Moon. *J. Geophys. Res.* **118**, 1435–1452 (2013).

21. Amsden, A. A., Ruppel, H. M., Hirt, C. W. SALE: A simplified ALE computer program for fluid flow at all speeds. **Report LA-8095**, (Los Alamos National Laboratory, Los Alamos, New Mex., 1980).

22. Collins, G. S., Melosh, H. J., Ivanov, B. A. Modeling damage and deformation in impact simulations. *Meteorit. Planet. Sci.* **39**, 27–231 (2004).

23. Wünnemann, K. and Collins, G. S. and Melosh, H. J. A strain-based porosity model for use in hydrocode simulations of impacts and implications for transient-crater growth in porous targets. *Icarus* **180**, 514–527 (2006).

24. Pierazzo, E., Artemieva, N. A., Ivanov, B. A. Starting conditions for hydrothermal systems underneath Martian craters: Hydrocode modeling. In *Large Meteorite Impacts III* (eds. Kenkmann, T., Hörz, F., Deutsch, A.), pp. 443-457, Spec. paper **384**, (Geological Society of America, Boulder, Colo., 2005).

25. Ivanov, B. A., Melosh, H. J., Pierazzo, E. Basin-forming impacts: Reconnaissance modeling, In *Large Meteorite Impacts and Planetary Evolution IV* (eds. Gibson, R. L., Reimold, W. U.), pp. 29–49, Spec. paper **465**, (Geological Society of America, Boulder, Colo., 2010).

26. Hüttig, C., Stemmer, K. Finite volume discretization for dynamic viscosities on voronoi grids. *Phys. Earth Planet. Inter.* **171**, 137–146 (2008).

27. Tera, F., Papanastassiou, D. A., Wasserburg, G. J. Isotopic evidence for a terminal lunar cataclysm. *Earth Planet. Sci. Lett.* **22**, 1–21 (974).

28. Kring, D. A., Cohen, B. A. Cataclysmic bombardment throughout the inner solar system 3.9–4.0 Ga. *J. Geophys. Res.* **107**, 5009 (2002).

29. Tsiganis, K., Gomes, R., Morbidelli, A., Levison, H. F. Origin of the orbital architecture of the giant planets of the solar system. *Nature* **435**, 459–461 (2005).

30. Williams, J.-P., Ruiz, J., Rosenburg, M. A., Aharonson, O., Phillips, R. J. Insolation driven variations of Mercury's lithospheric strength, *J. Geophys. Res.* **116**, E01008 (2011).

31. Fassett, C. I. *et al.* Large impact basins on Mercury: Global distribution, characteristics, and modification history from MESSENGER orbital data. *J. Geophys. Res.* **117**, E00L08 (2012).

32. Lawrence, D. J. *et al.* Small-area thorium features on the lunar surface. *J. Geophys. Res.* **108**, 5102 (2003).

33. Ito, T., Malhotra, R. Asymmetric impacts of near-Earth asteroids on the Moon. *Astron. Astrophys.* **519**, A63 (2010).

34. Gallant, J., Gladman, B., Ćuk, M. Current bombardment of the Earth-Moon system: Emphasis on cratering asymmetries. *Icarus* **202**, 371–382 (2009).

35. Wilhelms, D. E. The Geologic History of the Moon. *Professional Paper 1348*, U.S. Geological Survey, Denver, Colo., pp. 121–246 (1987).

36. Wieczorek, M. A., Le Feuvre, M. Did a large impact reorient the Moon? *Icarus* **200**, 358–366 (2009).

37. Frey, H. Previously unknown large impact basins on the Moon: Implications for lunar stratigraphy, in *Recent Advances and Current Research Issues in Lunar Stratigraphy* (eds. Ambrose, W. A., Williams, D. A.), Spec. Paper **477**, pp. 53–75, Geological Society of America, Boulder, Colo., 2011).

38. Pierazzo, E., Artemieva, N., Asphaug, E., Boldwin, E. C., Cazamias, J., Coker, R., Collins, G. S., Crawford, D. A., Davison, T., Elbeshausen, D., Holsapple, K. A., Housen, K. R., Krycansky, D. G., Wünnemann, K. Validation of numerical codes for impact and explosion cratering: Impacts on strengthless and metal targets. *Meteorit. Planet. Sci.* **43**, 1917–1938 (2008).

39. Davison, T. M., Collins, G. S., Elbeshausen, D., Wünnemann, K. & Kearley, A. Numerical modeling of oblique hypervelocity impacts on strong ductile targets. *Meteorit. Planet. Sci.* **46**, 1510–1524 (2011).

40. Bottke, W. F. *et al.*, An Archaean heavy bombardment from a destabilized extension of the asteroid belt. *Nature* **485**, 78–80 (2012).

41. Pierazzo, E., Melosh, H. J. Understanding oblique impacts from experiments, observations, and modeling. *Annu. Rev. Earth Planet. Sci.* **28**, 141–167 (2000).

42. Melosh, H. J., Freed, A. M., Johnson, B. C., Blair, D. M., Andrews-Hanna, J. C., Neumann, G. A., Phillips, R. J., Smith, D. E., Solomon, S. C., Wieczorek, M. A., Zuber, M. T. The origin of lunar mascon basins. *Science* **340**, 1552–1555 (2013).

43. Potter, R. W. K., Collins, G. S., Kiefer, W. S., McGovern, P. J., Kring, D. A. Constraining the size of the South Pole-Aitken basin impact. *Icarus* **220**, 730–743 (2012).

44. Ohnaka, M. A shear failure strength law of rock in the brittle-plastic transition regime. *Geophys. Res. Lett.* **22**, 25–28 (1995).

45. Ivanov, B., Melosh, H. J. Impacts do not initiate volcanic eruptions: Eruptions close to the crater. *Geology* **31**, 869–872 (2003).

46. Melosh, H. J., Ivanov, B. A. Impact crater collapse. *Annu. Rev. Earth Planet. Sci.* **27**, 385–415 (1999).

47. Collins, G. S., Melosh, H. J., Morgan, J. V. & Warner, M. R. Hydrocode simulations of Chicxulub crater collapse and peak-ring formation. *Icarus* **157**, 24–33 (2002).

48. Wünnemann, K., Ivanov, B. A. Numerical modelling of the impact crater depth-diameter dependence in an acoustically fluidized target. *Planet. Space Sci.* **51**, 831–845 (2003).

49. Collins, G. S., Morgan, J., Barton, P., Christeson, G. L., Gulick, S., Urrutia, J., Warner, M., Wünnemann, K. Dynamic modeling suggests terrace zone asymmetry in the Chicxulub crater is caused by target heterogeneity. *Earth Planet. Sci. Lett.* **270**, 221–230 (2008).

50. Lawrence, D. J. *et al.* Global elemental maps of the Moon: The Lunar Prospector gamma-ray spectrometer. *Science* **281**, 1484–1489 (1998).

51. Hirschmann, M. M. Mantle solidus: Experimental constraints and the effects of peridotite composition. *Geochem. Geophys. Geosyst.* **1**, 1042 (2000).

52. Spohn, T., Konrad, W., Breuer, D., Ziethe, R. The longevity of lunar volcanism: Implications of thermal evolution calculations with 2D and 3D mantle convection models. *Icarus* **149**, 54–65 (2001).

53. Amsden, A. A., Ruppel, H. M. SALE-3D: A Simplified ALE Computer Program for Calculating Three-Dimensional Fluid Flow. **Report LA-8095**, (Los Alamos National Laboratory, Los Alamos, New Mex., 1981).

54. Elbeshausen, D., Wünnemann, K., Collins, G. S. Scaling of oblique impacts in frictional targets: Implications for crater size and formation mechanism. *Icarus* **204**, 716–731 (2009).

55. Elbeshausen, D., Wünnemann, K. iSALE-3D: A three-dimensional, multi-material, multi-rheology hydrocode and its applications to large-scale geodynamic processes. *Proc. of 11th Hypervelocity Impact Symposium (HVIS)*, Fraunhofer Verlag (2011).